\



Lattice plasmon mode excitation via near-field coupling

Yun Lin(林蕴), Shuo Shen(申烁), Xiang Gao(高祥), and Liancheng Wang(汪炼成)
Citation: Chin. Phys. B, 2022, 31 (**1**): 014214. DOI: 10.1088/1674-1056/ac0523
Journal homepage: http://cpb.iphy.ac.cn; http://iopscience.iop.org/cpb

What follows is a list of articles you may be interested in

Plasmonic sensor with self-reference capability based on functional layer film composed of Au/Si gratings

Jiankai Zhu(朱剑凯), Xiangxian Wang(王向贤), Yunping Qi(祁云平), and Jianli Yu(余建立)
Chin. Phys. B, 2022, 31 (**1**): 014206. DOI: 10.1088/1674-1056/ac1335

A novel plasmonic refractive index sensor based on gold/silicon complementary grating structure

Xiangxian Wang(王向贤), Jiankai Zhu(朱剑凯), Yueqi Xu(徐月奇), Yunping Qi(祁云平), Liping Zhang(张丽萍), Hua Yang(杨华), and Zao Yi(易早)
Chin. Phys. B, 2021, 30 (**2**): 024207. DOI: 10.1088/1674-1056/abd690

An ultrafast and low-power slow light tuning mechanism for compact aperture-coupled disk resonators

Bo-Yun Wang(王波云), Yue-Hong Zhu(朱月红), Jing Zhang(张静), Qing-Dong Zeng(曾庆栋), Jun Du(杜君), Tao Wang(王涛), Hua-Qing Yu(余华清)
Chin. Phys. B, 2020, 29 (**8**): 084211. DOI: 10.1088/1674-1056/ab9df1

High-efficiency photon-electron coupling resonant emission in GaN-based microdisks on Si

Menghan Liu(刘梦涵), Peng Chen(陈鹏), Zili Xie(谢自力), Xiangqian Xiu(修向前), Dunjun Chen(陈敦军), Bin Liu(刘斌), Ping Han(韩平), Yi Shi(施毅), Rong Zhang(张荣), Youdou Zheng(郑有炓), Kai Cheng(程凯), Liyang Zhang(张丽阳)
Chin. Phys. B, 2020, 29 (**8**): 084203. DOI: 10.1088/1674-1056/ab9443

Oxide-aperture-dependent output characteristics of circularly symmetric VCSEL structure

Wen-Yuan Liao(廖文渊), Jian Li(李健), Chuan-Chuan Li(李川川), Xiao-Feng Guo(郭小峰), Wen-Tao Guo(郭文涛), Wei-Hua Liu(刘维华), Yang-Jie Zhang(张杨杰), Xin Wei(韦欣), Man-Qing Tan(谭满清)
Chin. Phys. B, 2020, 29 (**2**): 024201. DOI: 10.1088/1674-1056/ab5fbd

---

Lattice plasmon mode excitation via near-field coupling

Yun Lin(林蕴)[1,2], Shuo Shen(申烁)[1], Xiang Gao(高祥)[1], and Liancheng Wang(汪炼成)[1,†]

[1] *State Key Laboratory of High Performance Complex Manufacturing, College of Mechanical and Electrical Engineering, Central South University, Changsha* 410083, *China*

[2] *Xiangya School of Stomatology, Xiangya Stomatological Hospital, Central South University, Changsha* 410000, *China*

(Received 12 March 2021; revised manuscript received 22 May 2021; accepted manuscript online 26 May 2021)

The optical response of metal nanoparticles can be modified through near-field or far-field interaction, yet the lattice plasmon modes (LPMs) considered can only be excited from the latter. Here instead, we present a theoretical evaluation for LPM excitation via the near-field coupling process. The sample is an arrayed structure with specific units composed of upper metal disks, a lower metal hole and a sandwiched dielectric post. The excitation process and underlying mechanism of the LPM and the influence of the structure parameters on the optical properties have been investigated in detail by using a finite-difference time-domain (FDTD) numerical method. Our investigation presented here should advance the understanding of near-field interaction of plasmon modes for LPM excitation, and LPMs could find some potential applications, such as in near-field optical microscopes, biosensors, optical filters and plasmonic lasers.

Keywords: optical response of metal nanoparticles, lattice plasmon modes, finite-difference time-domain

PACS: 42.50.Gy, 42.30.Lr, 78.67.–n, 92.60.Ta **DOI:** 10.1088/1674-1056/ac0523

1. Introduction

Metal plasmonic materials have attracted intensive interest due to their wide potential applications including surface-enhanced Raman spectroscopy (SERS),[1] nanolithography,[2] biosensors,[3] thin film solar cells,[4] beam manipulations, nanolasers,[5] and color filters.[6,7] The optical response of a single metal particle is determined by its size, shape, composition, and local environment,[8] whereas this can be modified through near-field interaction by positioning metal nanoantennas in close proximity[9] or through far-field interaction by positioning the same particle in a regular array, i.e., diffraction effect.[10] Peter Nordlander has introduced a hybridization model for the plasmon response of complex nanostructures.[11] Since then, various nanocavity configurations have been proposed, such as ring/disk, dolmen, oligomer clusters, heptamer clusters and ring/rod nanostructures. Recently, structured lattices have been used to demonstrate superlattice resonances,[12,13] opening an extra route to manipulate optical properties. Nikitin[14–16] has theoretically and experimentally studied lattice plasmon modes (LPMs) originating from diffraction in periodic arrays of metal nanoparticles. Humphrey[17] has studied the lattice resonances in plasmonic arrays of asymmetric disc dimers. The Odom group has observed the lasing action of LPMs from the two-dimensional array of plasmonic Au or Ag surrounded by gain material.[18–21] The influence of size, shape, disorder, symmetry breaking and dielectric environment on the properties of LPMs has also been investigated.[22–26]

The above-mentioned LPMs are all excited through the diffraction effect. In order to activate the LPMs, the size of metal structure has to be small enough to make the energy of localized plasmon resonance (LPR) higher than that of the diffraction modes, which puts some limits on the structure design and nanofabrication. Here we present an approach to excite the LPMs via near-field coupling. We designed a coupled nanometal structure array and studied its optical responses in detail here. Our results could explain the abnormally increased transmission observed in Refs. [27–29], from Stephen Y. Chou's group. Various devices, such as sensors, color filters, emitters, and solid-state lighting, can be envisioned by using the proposed LPMs.[30–33]

2. Result and discussion

Electromagnetic properties of the designed nanometal structures were investigated by the method of three-dimensional (3D) finite-difference time-domain (FDTD) using the Lumerical software package. The structure (Al DK-HLs) consists of a glass substrate, an upper Al disk array (AlDKs) and a lower Al holes array (AlHLs), with a dielectric HSQ array (hydrogen silsesquioxane, $n = 1.47$) sandwiched in between. A plane wave with wavelength spanning from 300 nm–800 nm is incident from above and two-dimensional monitors are placed under and above the Al DK-HLs to record the electric field distributions of transmission (T) and reflection (R), respectively. The background refractive index is set to be 1 except where specially mentioned. The simulation area is discretized using a 3D grid mesh, with a step size of 6 nm in all the x-, y-, and z-directions. The material constants used for the structures in the simulation are silica (Palik), HSQ ($n = 1.41$), and Al (CRC Handbook of Chemistry and Physics). A peri-

†Corresponding author. E-mail: liancheng_wang@csu.edu.cn

© 2022 Chinese Physical Society and IOP Publishing Ltd

odic boundary condition is employed, with a rectangular unit cell consisting of one whole and four quarter spheres. The heights of AlDKs and AlHLs are both 30 nm.

Generally, when a plane wave with wave vector $\boldsymbol{k}_0$ is incident on a periodic array, it generates a number of diffracted orders with in-plane wave vector projections to be $\boldsymbol{K}_{p,q} = \boldsymbol{k}_{0,\parallel} + p\boldsymbol{G}_x + q\boldsymbol{G}_y$, with $\boldsymbol{k}_{0,\parallel}$ to be the in-plane component of $\boldsymbol{k}_0$, and $\boldsymbol{G}_x = (2\pi/a_x)\boldsymbol{e}_x$ and $\boldsymbol{G}_y = (2\pi/a_y)\boldsymbol{e}_y$ to be the reciprocal lattice vectors. The wave number along the z axis is thus determined as $\boldsymbol{k}_{p,q} = \sqrt{(2\pi n/\lambda)^2 - K_{p,q}^2}$ $(\boldsymbol{k}_0 = 2\pi n/\lambda)$ for diffraction into material with refractive index of n. If $2\pi n/\lambda < K_{p,q}$, $\boldsymbol{k}_{p,q}$ is imaginary, corresponding to the evanescent order; otherwise, if $2\pi n/\lambda > K_{p,q}$, $\boldsymbol{k}_{p,q}$ is real, corresponding to propagating diffraction order. For $(+1, 0)$ or $(-1, 0)$ orders, the critical λ for transition from evanescent state to propagating state, equally speaking, the Rayleigh anomaly or diffraction edge, is located at $\lambda_{\mathrm{RA}} = na_x$. For a periodical metal lattice, such as AlDKs, $\lambda_{\mathrm{LPR}} < \lambda_{\mathrm{RA}}$ satisfies when the periodicity is relatively larger and the radius of the Al nanodisk is relatively smaller. LPR then collectively couples into the propagating diffraction order, exhibiting a sharp and strong feature, that is the LPM, in the transmission spectrum. LPM is inhibited when $\lambda_{\mathrm{LPR}} > \lambda_{\mathrm{RA}}$, due to the evanescent characteristics.

Figure 1(a) sketches the structure (Al DK-HLs) under investigation. AlDKs, HSQ and AlHLs have the same radius (R) and periodicity (P), and the height of HSQ is H. The inset of Fig. 1(a) sketches the cross section of the unit Al DK-HLs. We purposely decomposed the Al DK-HLs and investigated the optical properties of each component, i.e., AlDKs, AlHLs, and their combinations. The periodicity and radius are purposely chosen with (b) $P = 520$ nm, $R = 60$ nm and (c) $P = 420$ nm, $R = 100$ nm, respectively, to locate λ_{RA} at the short and long wavelength side of λ_{LPR}, corresponding to the diffraction and near filed region, respectively. The diffraction edge (denoted as blue dashed line) and LPR (denoted as black dashed line) are located at (b) $\lambda_{\mathrm{RA}} = 639$ nm, $\lambda_{\mathrm{LPR}} = 500$ nm and (c) $\lambda_{\mathrm{RA}} = 516$ nm, $\lambda_{\mathrm{LPR}} = 650$ nm, respectively. At diffraction region (Fig. 1(b)), the transmission lineshape of AlDKs+HSQ (red line) exhibits a sharp and narrow LPM dip at $\lambda = 680$ nm, with the transmission modulation depth to be 0.38, along with a broad and relatively weak LPR dip centered at $\lambda \sim 500$ nm. LPM exhibits as a peak at $\lambda = 674$ nm in the transmission spectrum (blue line) of AlHLs, exhibiting much lower intensity compared with surface plasmon polaritons (SPP) mode, which is located at ~ 500 nm. Note that transmission through Al DK-HLs ($H = 100$ nm) is significantly enhanced to be 0.38 at the LPM position (with transmission is 0.06 for AlHLs), even though all holes of AlHLs are blocked by the metal disks with zero projected open area in AlDKs. The transmission peak intensity decreases when the height of the dielectric HSQ is decreased to 40 nm (green line, Fig. 1(b)).

Nikitin *et al.*[14–16] have investigated the spectral characteristics of AlDKs at the diffraction region; we concentrate more on the near-field coupling region here. At the near-field region (Fig. 1(c)), the transmission lineshape for AlDKs+HSQ, red line, (AlHLs, blue line) consists of a faint peak (dip) and a dominantly much broader dip (peak), corresponding to the Rayleigh anomaly and LPR (SPP), respectively. Note that AlHLs could also support LPR resonances. The faint dip (peak) located within the Rayleigh anomaly region is considered to be LPM, which is quite weak due to its evanescent characteristics. Compared with sole AlDKs (AlHLs), an addition of dielectric HSQ, i.e., AlDKs + HSQ (AlHLs + HSQ) red shifts the spectrum and simultaneously intensifies (weakens) the LPMs. The Al DK-HLs ($H = 100$ nm) exhibits an obvious LPM peak besides the dominant peak (antibonding symmetrical mode (SM)) in the visible wavelength region. The SM mode will be discussed later. When H is decreased to 40 nm, the intensity of SM decreases and converges with LPM. The LPM lineshape exhibits a typical asymmetrical Fano feature when $H = 100$ and 40 nm. Compared with the AlDKs+AlHLs structure (i.e., Al DK-HLs without HSQ), LPM is much stronger in the Al DK-HLs (not shown), suggesting that the HSQ intensifies the process of energy channelling to LPMs, even though it red shifts the SM and makes LPM and SM more separated.

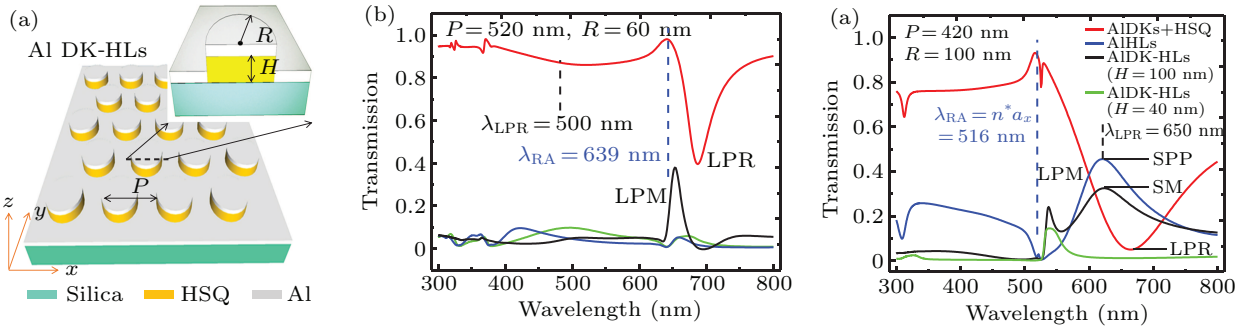


Fig. 1. Panel (a) sketches the structure (Al DK-HLs) under investigation, with periodicity P, radius R and height H. The inset of (a) sketches the cross section of the structure unit. Optical properties of AlDK-HLs and its component at (b) diffraction region with $P = 520$ nm, $R = 60$ nm and (c) near-field interaction region with $P = 420$ nm, $R = 100$ nm.

We then investigate the optical properties of the Al DK-HLs by systematically varying the structural parameters. Figure 2(a) shows transmission spectra of Al DK-HLs with (a1) $P = 420$ nm, $H = 100$ nm and (a2) $P = 420$ nm, $H = 40$ nm, and varied radius R. As shown in Fig. 2(a1), when R increases, SM red shifts and LPM shows a negligent shift. When $H = 40$ nm, LPM and SM are almost overlapped at varied R, indicating that strong coupling happens between LPM and SM, regardless of the radius R. We then varied the height of HSQ (H) at the near-field region with $P = 420$ nm, $R = 100$ nm (b1), and at the diffractive region with $P = 520$ nm, $R = 60$ nm (b2), respectively. When H decreases, SM blue shifts and moves closer to LPM, resulting in an intensified coupling strength. When $H = 40$ nm, SM almost overlaps with LPM and the spectrum is dominated by the LPM peak, exhibiting an almost standard Lorentzian profile. It is speculated that the height of HSQ influences LPM via two routes: (I) SM mode blue shifts and moves closer to LPM when H decreases, thus energy is more efficiently channeled into LPM; (II) LPMs from top AlDKs and bottom AlHLs interact more efficiently when H decreases due to evanescent feature of LPMs at the near-field region. For $P = 520$ nm, $R = 60$ nm, the spectra show a dominant peak at the diffraction edge. However, the dominant peak feature vanishes when $H = 40$ nm, which is contrary to the phenomenon observed at the near-field region (Fig. 2(b)). The environmental refractive index was further varied, as shown in Figs. 2(c1) and 2(c2). Since the diffraction edge is determined by $\lambda_{RA} = na_x$, LPMs red shift with $\lambda_{LPM} = 361$ nm, 528 nm and 667 nm when $n = 1$, 1.4, 1.8 as expected, when $P = 420$ nm, $R = 100$ nm and $H = 100$ nm. For $H = 40$ nm, the dominant LPM peak remains, and it red shifts with a decreased intensity as n increases. The positions of LPM roughly follow the trend set by $\lambda_{RA} = na_x$ for both $H = 40$ nm and $H = 100$ nm cases. For example, for $n = 1$ (1.4), the positions of LPM are roughly calculated to be $420\sqrt{3}/2 = 363$ nm ($420\sqrt{3}/2 \cdot 1.4 = 509$ nm). The slight deviation of simulated and calculated LPM peak is due to the coupling effect from the top AlDKs and bottom AlHLs. Note that the refractive index of HSQ is fixed, which has been found to have negligible influence on the position and lineshape of LPMs (not shown here). The periodicity of Al DK-HLs is varied subsequently, which is expected to be strongly relevant with LPM position ($\lambda_{RA} = na_x$). R is varied purposely to locate LPMs within the near-field coupling region, i.e., $\lambda_{LPR} > \lambda_{RA}$. As shown in Fig. 2(d), the transmission spectra feature shows an obvious difference for $H = 100$ and 40 nm at varied P: there is a dominant peak at the corresponding LPM position when $H = 40$ nm, and modes are de-overlapped when $H = 100$ nm. LPM position generally follows $\lambda_{RA} = na_x$. It is revealed from the analysis above that strong near-field coupling could happen only when the top AlDKs are spatially close enough to the AlHLs, independent of the radius, environmental refractive index and periodicity.

We further analyzed the field distribution for LPM, SM and ASM (anti-symmetric mode). Figures 3(a) and 3(b) plot the transmission and reflection spectra for AlDK-HLs with $P = 420$ nm, $R = 100$ nm and varied H. Figure 3(e) summarizes the energy positions of LPM, ASM and SM as a function of H. It is clearly observed that, when H decreases, SM and ASM mode blue and red shifts, respectively, whereas LPM remains almost unvaried. Figures 3(c) and 3(d) plot the electric field distribution of SM and ASM along the XZ cross section.

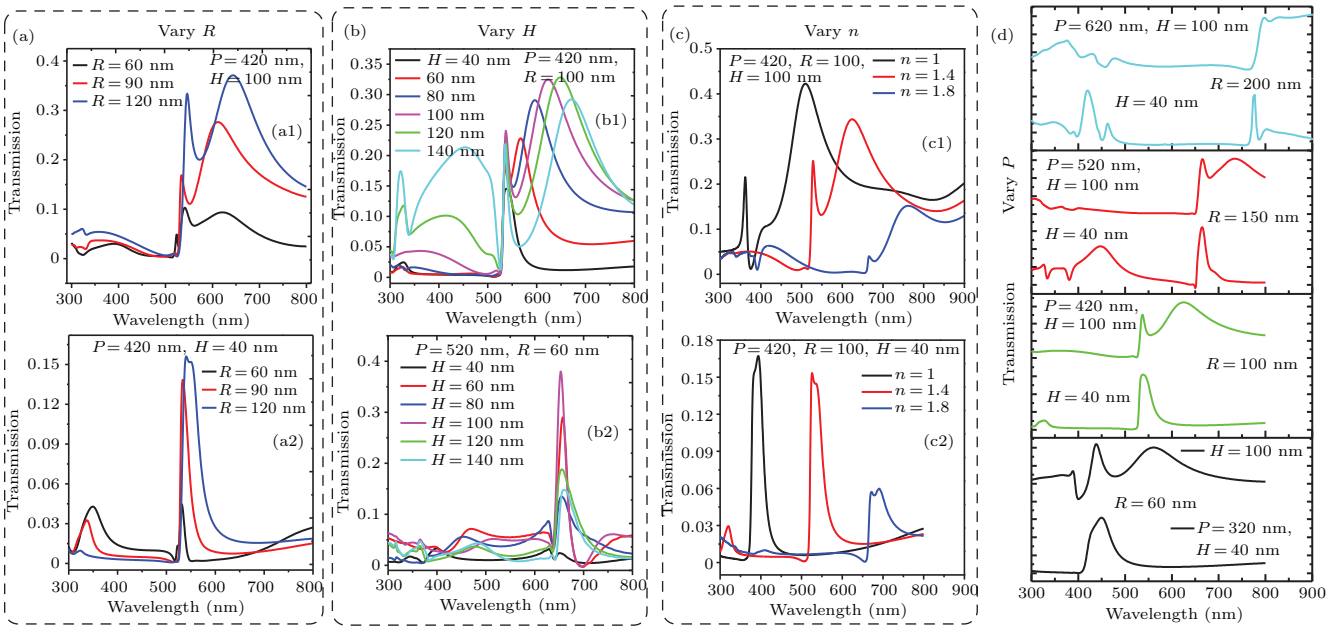


Fig. 2. Optical transmission properties of the Al DK-HLs with systematically varied structural parameters: (a) varied radius R, (a1) $P = 420$ nm, $H = 100$ nm, (a2) $P = 420$ nm, $H = 40$ nm; (b) varied height of HSQ (H) for (b1) near-field coupling region with $P = 420$ nm, $R = 100$ nm, and (b2) diffractive coupling region with $P = 520$ nm, $R = 60$ nm; (c) varied environment refractive index n; (d) varied lattice periodicity P.

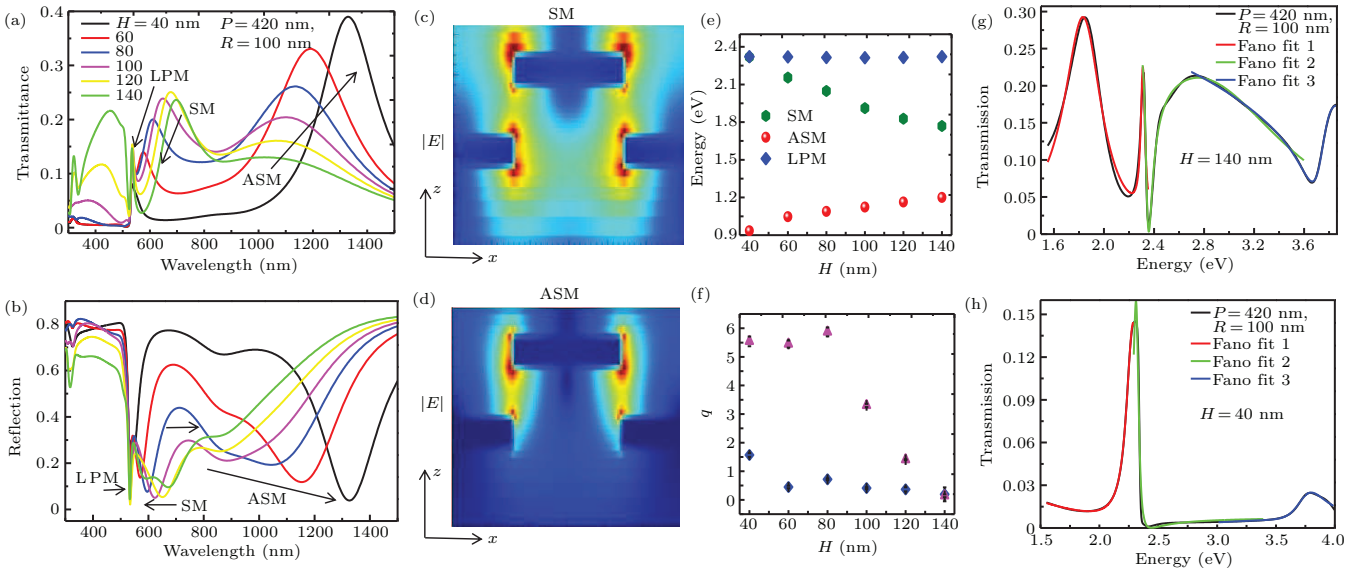


Fig. 3. (a) Transmission and (b) reflection spectra in the full wavelength region for Al DK-HLs with $P = 420$ nm, $R = 100$ nm and varied H; the electric field distribution of (c) SM and (d) ASM modes in the XZ cross section; (e) the energy position of LPM, ASM and SM as a function of H; (g) and (h) the transmission spectral of Al DK-HLs ($P = 420$ nm, $R = 100$ nm) with $H = 100$ nm and 40 nm; (f) summarizes the q value for the three sections in (g) and (h).

It is observed that the electric field is concentrated between the top metal disk and bottom metal hole for ASM, whereas it is pushed outward for the SM mode, indicating the asymmetric bonding and symmetric antibonding features for the ASM and SM modes, respectively. The energy of the SM mode and incident light are channeled into LPM. Equally speaking, the broad SM mode and incident light couple with the relatively narrower LPM, resulting in a typical asymmetrical Fano lineshape. Figures 3(g) and 3(h) plot the transmission spectra of Al DK-HLs ($P = 420$ nm, $R = 100$ nm) when $H = 100$ nm and 40 nm. The spectra with a Fano-like asymmetric line shape could be expressed as[34,35]

$$\sigma_{\mathrm{a}}(\omega) = \frac{\left(\dfrac{\omega^2 - \omega_{\mathrm{a}}^2}{2\omega_{\mathrm{a}} W_{\mathrm{a}}} + q\right)^2 + b}{\left(\dfrac{\omega^2 - \omega_{\mathrm{a}}^2}{2\omega_{\mathrm{a}} W_{\mathrm{a}}}\right)^2 + 1}, \tag{1}$$

$$\sigma_{\mathrm{s}}(\omega) = \frac{a^2}{\left(\dfrac{\omega^2 - \omega_{\mathrm{s}}^2}{2\omega_{\mathrm{s}} W_{\mathrm{s}}}\right)^2 + 1}, \tag{2}$$

where ω_{a} is the central position of resonance, W_{a} is an approximation of its spectrum width in frequency units, q is the asymmetry parameter, and b is the modulation damping parameter originating from intrinsic losses. The resonance strength of the broad mode follows a symmetric pseudo-Lorentzian line shape as a function of the frequency ω, where a is the maximum amplitude of the resonance, ω_{s} is the resonance frequency, and W_{s} is an approximation of its spectrum width in frequency units for ω_{s}. The resonance strength of the entire system is given by the product of the symmetric resonance (SR) σ_{s} with the asymmetric resonance (AR) σ_{a}, as shown in the following equation:

$$\sigma_{\mathrm{t}}(\omega) = \sigma_{\mathrm{s}}(\omega)\sigma_{\mathrm{a}}(\omega). \tag{3}$$

We used the above equation to fit the lineshape separated into three sections I, II and III, corresponding to red, green and blue lines in Figs. 3(g) and 3(h), respectively. The asymmetry parameter q characterizes the energy transfer direction: in the limit of $q \to \infty$, the transition to the continuum is weak, and the lineshape is entirely determined by the transition to the discrete state; when $q \to 0$, the transition to the discrete state is weak; when $q \to 1$, the transitions to the discrete and continuum states are almost equal. A larger q indicates that more energy is channeled into the discrete LPM state. Figure 3(f) summarizes the q value for the three sections as a function of H. q increases when H is decreased, indicating that the probability of transition to the discrete LPM state increases. The interaction between the LPM, ASM and SM modes can be simply and qualitatively summarized as the following Hamiltonian matrix:

$$\hat{H} = \begin{bmatrix} \mathrm{ASM} & \Delta E & 0 \\ \Delta E & \mathrm{SM} & q(\Delta E) \\ 0 & q(\Delta E) & \mathrm{SLP} \end{bmatrix}. \tag{4}$$

The near-field coupling strength is determined by the energy separation, which is further dependent on dielectric height H.

Based on the above analysis, the process for the optical transmission in the near-field region for AlDK-HLs is summarized as illustrated in Fig. 4: LPR and SPP in AlDKs and AlHLs and weak LPMs in the relatively wider RA regions are excited by the incident light. LPR and SPP couple with each other, resulting in the formation of a low-energy ASM and a high-energy SM. ASM extends to the infrared region

and SM further couples with LPMs via near-field interaction. When the separation between the AlDKs and AlHLs becomes smaller, coupling is intensified, resulting in a dominant quasi-single LPM peak in the visible region. Chou[20] reported an extraordinary light transmission through Al DK-HLs, which is considered to be located at the diffraction region; instead, LPMs in this scenario are excited via evanescent mode near-field coupling.

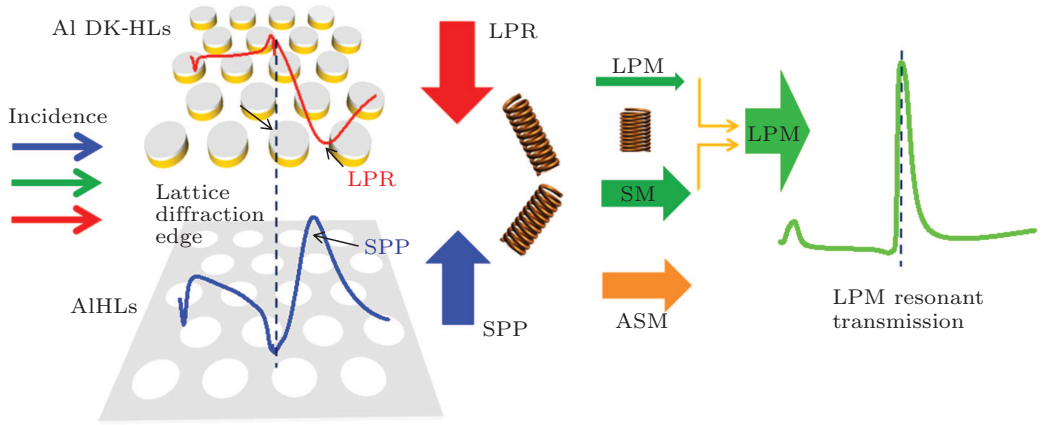


Fig. 4. Mechanism of LPM excitation: LPR and SPP in AlDKs and AlHLs are excited by the incident light, couple with each other, resulting in a low-energy ASM and a high-energy SM. SM further couples with LPMs via near field interaction, resulting in a dominant quasi-single peak transmission LPM peak in the visible region.

3. Conclusion

To conclude, we have analyzed LPM excitation at the near-field region in an arrayed structure composed of paired upper AlDKs and lower AlHLs. The excitation process, mechanism and the influence of the structure parameters, including the radius, post height, environmental refractive index and periodicity, have been investigated in detail through FDTD simulation. The LPM originates from the near-field coupling between LPR from the upper AlDKs and SPP from the lower AlHLs, which depends on the gap distance and is independent of the radius, environmental refractive index and periodicity of the structure. This renders the LPM excited at the near-field region advantages of increased tolerance on nanofabrication process. The study presented here renders a deeper understanding on near-field interaction between plasmon modes, and LPMs may find potential applications in various areas, including near-field optical microscopes, chemical sensing, novel optical filters, and plasmonic lasers.

Acknowledgements

Project supported by Key Laboratory of Energy Conversion and Storage Technologies (Southern University of Science and Technology), Ministry of Education, Shenzhen, China, the National Key Research and Development Program of China (Grant No. 2018YFB0406702), Professorship Start-up Funding (Grant No. 217056), Innovation-Driven Project of Central South University (Grant No. 2018CX001), Project of State Key Laboratory of High Performance Complex Manufacturing, Central South University (Grant No. ZZYJKT2018-01).

References

[1] Willets K A and Van Duyne R P 2007 *Ann. Rev. Phys. Chem.* **58** 267
[2] Jensen T R, Malinsky M D, Haynes C L and Van Duyne R P 2000 *J. Phys. Chem. B* **104** 10549
[3] Zhao J, Zhang X, Yonzon C R, Haes A J and Van Duyne R P 2006 *Nanomedicine* **1** 219
[4] Atwater H A and Polman A 2010 *Nat. Mater.* **9** 205
[5] Oulton R F, Sorger V J, Zentgraf T, Ma R M, Gladden C, Dai L and Zhang X 2009 *Nature* **461** 629
[6] Wang L, Ng R J H, Safari Dinachali S, Jalali M, Yu Y and Yang J K 2016 *ACS Photon.* **3** 627
[7] Yokogawa S, Burgos S P and Atwater H A 2012 *Nano Lett.* **12** 4349
[8] Pelton M, Aizpurua J and Bryant G 2008 *Laser Photon. Rev.* **2** 136
[9] Wang L, Liu Z, Yi X, Zhang Y, Li H, Li J and Wang G 2016 *J. Appl. Phys.* **119** 173106
[10] Vakevainen A I, Moerland R J, Rekola H T, Eskelinen A P, Martikainen J P, Kim D H and Törmä P 2014 *Nano Lett.* **14** 1721
[11] Prodan E, Radloff C, Halas N J and Nordlander P 2003 *Science* **302** 419
[12] Auguié B and Barnes W L 2008 *Phys. Rev. Lett.* **101** 143902
[13] Kravets V G, Schedin F and Grigorenko A N 2008 *Phys. Rev. Lett.* **101** 087403
[14] Nikitin A G 2014 *Appl. Phys. Lett.* **104** 061107
[15] Nikitin A G, Nguyen T and Dallaporta H 2013 *Appl. Phys. Lett.* **102** 221116
[16] Nikitin A G, Kabashin A V and Dallaporta H 2012 *Opt. Express* **20** 27941
[17] Humphrey A D, Meinzer N, Starkey T A and Barnes W L 2016 *ACS Photon.* **3** 634
[18] Zhou W, Dridi M, Suh J Y, Kim C H, Co T D, Wasielewski M R and Odom T W 2013 *Nat. Nanotech.* **8** 506
[19] Gao H, Zhou W and Odom T W 2010 *Adv. Funct. Mater.* **20** 529
[20] Zhou W, Hua Y, Huntington M D and Odom T W 2012 *J. Phys. Chem. Lett.* **3** 1381
[21] Zhou W and Odom T W 2011 *Nat. Nanotech.* **7** 423
[22] Kelly K L, Coronado E, Zhao L L and Schatz G C 2003 *J. Phys. Chem. B* **107** 668

[23] Mock J J, Barbic M, Smith D R, Schultz D A and Schultz S J 2002 *Chem. Phys.* **116** 6755
[24] Auguié B and Barnes W L 2009 *Opt. Lett.* **34** 401
[25] Humphrey A D and Barnes W L 2014 *Phys. Rev. B* **90** 075404
[26] Christ A, Martin Q J, Ekinci Y, GippiusN A and Tikhodeev S G 2008 *Nano Lett.* **8** 2171
[27] Li W D, Hu J and Chou S Y 2011 *Opt. Express* **19** 21098
[28] Li W D, Ding F, Hu J and Chou S Y 2011 *Opt. Express* **19** 3925
[29] Chen Q and Cumming D R 2010 *Opt. Express* **18** 14056
[30] Zhang S, Genov D A, Wang Y, Liu M and Zhang X 2008 *Phys. Rev. Lett.* **101** 047401
[31] Thackray B D, Kravets V G, Schedin F, Auton G, Thomas P A and Grigorenko A N 2014 *ACS Photon.* **1** 1116
[32] Vecchi G, Giannini V and Gómez Rivas J 2009 *Phys. Rev. Lett.* **102** 146807
[33] Lozano G, Louwers D J, Rodríguez S R K, Murai S, Jansen O T A, Verschuuren M A and Gómez Rivas 2013 *Light: Sci. Appl.* **2** e66
[34] Miroshnichenko A E, Flach S and Kivshar Y S 2010 *Rev. Mod. Phys.* **82** 2257
[35] Lukýanchuk B, Zheludev N I, Maier S A, Halas N J, Nordlander P, Giessen H and Chong C T 2010 *Nat. Mater.* **9** 707